





Numerical investigation of multistability in the unstable flow of a polymer solution through porous media

Manish Kumar ¹, Soroush Aramideh,¹ Christopher A. Browne ²,
Sujit S. Datta ² and Arezoo M. Ardekani ¹

¹*Department of Mechanical Engineering, Purdue University, 585 Purdue Mall,
West Lafayette, Indiana 47907, USA*

²*Chemical and Biological Engineering, Princeton University, Princeton, New Jersey 08544, USA*



(Received 19 June 2020; accepted 4 March 2021; published 25 March 2021)

The flow of viscoelastic polymeric fluids through porous media is common in industrial applications such as oil recovery and groundwater remediation. Polymeric stresses can lead to an elastic-induced instability of the flow. Here, we numerically study the flow of a polymeric fluid in a channel consisting of multiple diverging and converging physical constraints, mimicking the pore bodies and throats of an ordered porous medium. Inertial stresses here are negligible, and instead the flow is dominated by elasticity and viscosity; their relative effects are characterized by the Weissenberg number. There is a critical Weissenberg number below which eddies appear on the top and the bottom of each pore. Above the critical Weissenberg number, eddies form in different regions of the pores and multiple distinct unstable flow structures occur. The stretched polymeric chains inside the pore facilitate eddy formation, whereas relaxed chains lead to eddy-free regions. We quantify the eddy area and correlations between the flow patterns of different pairs of pores, as well as polymeric stress and pressure drop across the tortuous channel to better understand the mechanism behind the observed flow patterns.

DOI: [10.1103/PhysRevFluids.6.033304](https://doi.org/10.1103/PhysRevFluids.6.033304)

I. INTRODUCTION

Polymers can impart elastic properties to fluids, producing non-Newtonian spatiotemporal flow features [1–5]. Understanding polymer flow in porous media is of particular importance for enhanced oil recovery (EOR) [6] and groundwater remediation [7,8], where polymer additives have improved the displacement of trapped nonaqueous liquids for collection downstream [9–14]. The flow of viscoelastic mucus through arrays of pillars (2D porous media) is also important for the transport of gametes and embryos in the reproductive track [15] and the trapping of inhaled dust particles in the airways of lungs [16]. In confined geometries, the surrounding porous matrix strongly affects the spatial and temporal features of the flow [17–21]. For example, the presence of polymers can induce strong velocity fluctuations, locally increasing viscous forces, and subsequently promoting the displacement of trapped liquids [22–26]. Understanding the spatiotemporal details of these flow fluctuations is important for effective EOR and groundwater remediation, but also for other emerging applications such as controlling mixing and flow in laboratory-on-a-chip devices, filtration [27], and extrusion of polymeric resins during 3D printing [28,29]. However, the onset of flow instabilities and the resulting flow features are highly sensitive to polymer properties, flow geometry, and imposed flow conditions [30–32]. This sensitivity challenges experimental observations, leaving many open questions on how to control the flow structure for fluid recovery [1,23,24,33–39].

Between the solid grains of a porous matrix, there are large bodies of fluid-filled void space, connected to neighboring pore bodies by relatively small throats. These bodies and throats are often modeled with a series of expansions and constrictions [17,40–42]. Upstream of constrictions, persistent recirculating eddies often form [43–48] to minimize the extensional stresses associated with polymer chain alignment [49–53]. Polymers are elongated by these curved streamlines, relaxing on a characteristic timescale λ . For sufficiently high shear rates $\dot{\gamma}$, polymers are advected faster than they relax, producing strong flow fluctuations at high Weissenberg numbers $Wi \equiv \lambda\dot{\gamma}$ [54–58]. This fluctuating flow is sometimes called “elastic turbulence” because its features are often reminiscent of traditional inertial turbulence [55–57], despite the absence of inertia, characterized by arbitrarily small Reynolds numbers $Re \ll 1$.

Microfluidic experiments have revealed a variety of complex spatiotemporal flow features produced by these instabilities [45,46,59–75]. However, in 3D porous media—like those encountered in EOR and groundwater remediation—the role of higher connectivity, elevated disorder, and successive pores are expected to significantly alter the flow [21,33,34,76–82]. In particular, the accumulation of stresses as polymers traverse successive pores can produce spatial variation in the dominant flow features [43,44,63,64,83,84]. In the interesting case of dense pores, polymers are advected faster than they relax, kinetically trapping polymers within each pore. Surprisingly, this trapping can produce a bistability in the flow, where each pore switches stochastically between two distinct flow structures: an eddy-dominated structure and an eddy-free structure [47]. The emergence of multiple persistent flow structures is consistent with some theoretical predictions [45,85,86] and is hypothesized to occur when polymers within a pore are locally kinetically trapped in an extended or coiled conformation, respectively, and hence when polymers’ advection timescale is smaller than relaxation timescale. However, the details of how these structures arise are unclear, and the role of spatial and temporal correlations between pore-scale flow structures are still largely unknown. Despite advances in imaging single-polymer conformations [2,64,87–94], microscopic flow details remain hard to access experimentally in highly unstable flow.

Here, we uncover the underlying physical mechanisms of this multistability using numerical simulations. We are able to directly probe the local stress fields, elucidating the physical mechanisms underlying flow structures. We further observe a new, relatively rare flow structure, where eddies transiently appear in the center of pores, prompting new experimental investigations. Finally, we probe spatial correlations on shorter timescales and longer length scales than possible experimentally, showing that weak positive correlations in flow structures can persist for many pores. These results help elucidate how the local accumulation of extensional stresses contribute to the formation of various persistent flow structures in unstable polymer solution flow. Understanding and controlling these multistable flow structures may aid the application of these flows to EOR, groundwater remediation, laboratory-on-a-chip devices, filtration, and 3D printing technologies.

II. PROBLEM SETUP

In this work, we investigate the flow of viscoelastic fluid through a pore constriction array by performing two dimensional numerical simulations. The geometry used in the simulation to investigate the elastically induced instability is a channel of width W with wall-centered pillar obstructions with diameter D (Fig. 1). The center-to-center separation of these pillars in the x -direction is varied from $l_s = W$ for 10 closely spaced pores [Fig. 1] to $l_s = 8W$ for two widely spaced pore throats [Fig. 5(a)]. We also study the flow behavior in a single-pore throat channel made of a single pair of wall-centered pillars [Fig. 2(a)]. The Reynolds number (Re) and Weissenberg number (Wi) are the relevant dimensionless numbers. Re represents the ratio of inertial to viscous stresses and is given as $Re = \rho U_t L_t / \eta$, where η is zero-shear rate viscosity, ρ is fluid density, U_t is the average fluid velocity through the throat of the pore and length scale L_t is the half-width of the pore throat [95]. Wi represents the ratio of elastic to viscous stresses and has been defined as

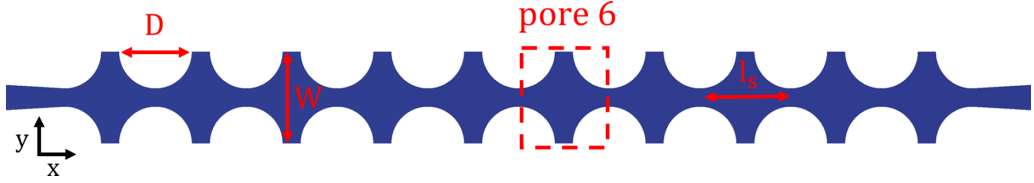


FIG. 1. The geometry used for numerical simulations. $D = 1.6$ mm is the diameter of the pillar and $W = 2$ mm is the width of the channel. The region enclosed with the square box depicts a sample pore.

$Wi = N_1/2\tau_w$, where N_1 is the first normal stress difference and τ_w is the shear stress. To estimate Wi , we use a planar rectilinear flow of a shear-thinning fluid obeying the FENE-P constitutive model through a slit of width same as the width of pore throat [95] and calculate Wi corresponding to the shear stress at the wall of the channel [96]. We use the time required to inject a single-pore throat volume fluid as the characteristic timescale, $t_{pv} = V_{pv}/Q$, where $V_{pv} = DW - \pi D^2/4$ is the pore throat volume per unit depth and Q is the volumetric flow rate per unit depth of the channel.

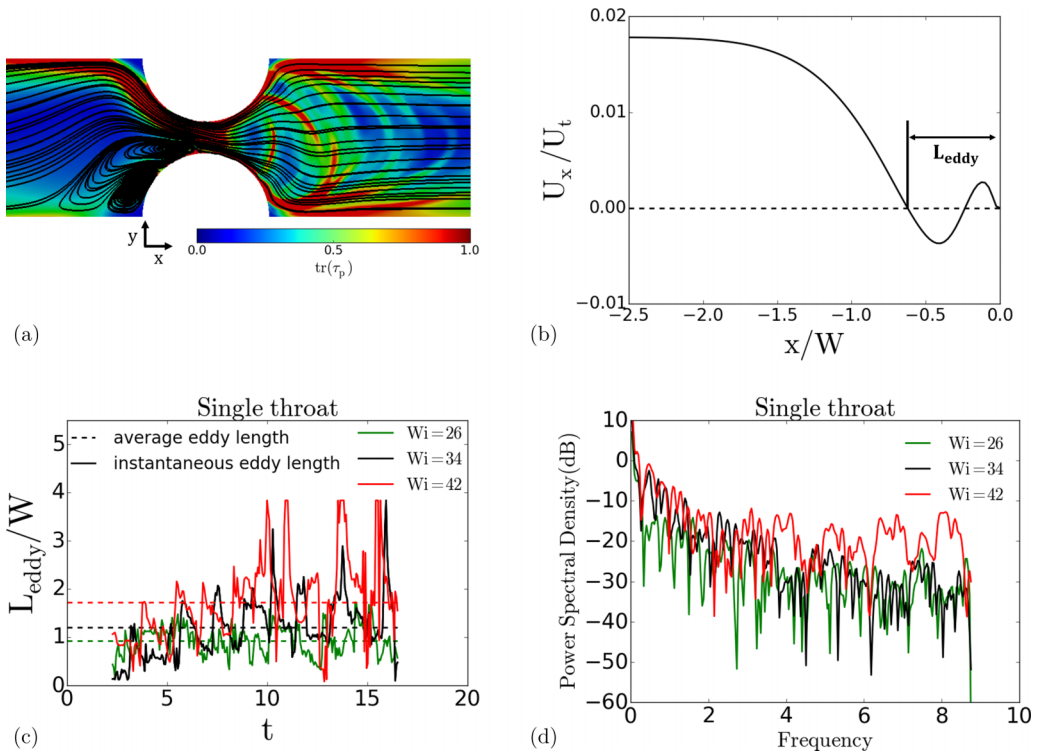


FIG. 2. (a) The streamlines depicting the eddies formation in the upstream of a single throated channel at $Wi = 26$. The contour represents the trace of polymeric stress tensor in the channel. (b) x -component of velocity along the length of channel close to the wall (at a distance $\Delta y/W = 0.015$ from the wall, where Δy is the height of first grid element next to the wall). (c) The instantaneous and time-averaged length of eddies at different Wi in the upstream of a single-pore channel. The time is nondimensionalized with timescale t_{pv} . (d) Power spectral density (PSD) of the normalized eddies' length (L_{eddy}/W). Frequency is normalized with $1/t_{pv}$.

III. GOVERNING EQUATIONS

The transient flow behavior of the incompressible fluid is governed by the conservation of mass and momentum:

$$\nabla \cdot \mathbf{u} = 0, \quad (1)$$

$$\rho \left(\frac{\partial \mathbf{u}}{\partial t} + \mathbf{u} \cdot \nabla \mathbf{u} \right) = -\nabla p + \nabla \cdot \boldsymbol{\tau}, \quad (2)$$

where \mathbf{u} , p and $\boldsymbol{\tau}$ are the flow field, pressure field and total stress tensor, respectively. The stress tensor $\boldsymbol{\tau}$ consists of solvent stress $\boldsymbol{\tau}_s$ and polymeric stress $\boldsymbol{\tau}_p$, $\boldsymbol{\tau} = \boldsymbol{\tau}_s + \boldsymbol{\tau}_p$. The solvent stress tensor, $\boldsymbol{\tau}_s$, can be obtained as $\boldsymbol{\tau}_s = \eta_s(\nabla \mathbf{u} + \nabla \mathbf{u}^T)$, where η_s is the solvent viscosity. We use the FENE-P constitutive equation to calculate the polymeric stresses [76,97]:

$$\boldsymbol{\tau}_p + \frac{\lambda}{f} \overset{\nabla}{\boldsymbol{\tau}}_p = \frac{a\eta_p}{f} (\nabla \mathbf{u} + \nabla \mathbf{u}^T) - \frac{D}{Dt} \left(\frac{1}{f} \right) [\lambda \boldsymbol{\tau}_p + a\eta_p \mathbf{I}], \quad (3)$$

where λ is the relaxation time of the polymer, η_p is the polymeric contribution to zero-shear rate viscosity $\eta = \eta_s + \eta_p$, \mathbf{I} is identity tensor, and $\frac{D}{Dt}$ is the material derivative. Function f is given as

$$f(\boldsymbol{\tau}_p) = \frac{L^2 + \frac{\lambda}{a\eta_p} \text{tr}(\boldsymbol{\tau}_p)}{L^2 - 3}, \quad (4)$$

where $a = L^2/(L^2 - 3)$ and parameter $L^2 = 3R_0^2/R_e^2$ measures the extensibility of the polymer chains [96,97]. R_0 is the maximum allowable length of the polymeric chain and R_e characterizes the equilibrium length of the chain. A typical range of the parameter L^2 found in the literature for FENE-P model is 10-1000 [76,95,97,98] and FENE-P model reduces into an Oldroyd-B constitutive model in the limit of $L^2 \rightarrow \infty$. Operator $\overset{\nabla}{\boldsymbol{\tau}}$ used in equation (3) represents the upper convective time derivative and is given by

$$\overset{\nabla}{\boldsymbol{\tau}}_p = \frac{D\boldsymbol{\tau}_p}{Dt} - \boldsymbol{\tau}_p \cdot \nabla \mathbf{u} - \nabla \mathbf{u}^T \cdot \boldsymbol{\tau}_p. \quad (5)$$

The numerical simulations are performed using a finite volume model using an open-source framework OpenFOAM [99] integrated with RHEOTOOL [100]. The equations are discretized using the finite volume method and the log-conformation approach has been used to calculate the polymeric stress tensor with higher accuracy and robustness. The relation between the polymeric stress tensor and conformation tensor is given as

$$\boldsymbol{\tau}_p = \frac{\eta_p}{\lambda} (f e^{\boldsymbol{\Theta}} - a\mathbf{I}), \quad (6)$$

where $\boldsymbol{\Theta}$ is the logarithm of conformation tensor. The details of the numerical methodologies and the code validations can be found here [100,101]. In our simulations, we change the relaxation time (λ) from 0.02 to 0.5 s to change Wi , while keeping $\rho = 1 \text{ kg/m}^3$, $\eta_p = 0.99 \text{ Pa s}$, $\eta_s = 0.01 \text{ Pa s}$, $L^2 = 625$, and volumetric flow rate per unit depth of the channel $Q = 16.8 \text{ mm}^2/\text{s}$ constant throughout the study. The width of the pore throat is $2L_t = 0.4 \text{ mm}$ and the average fluid velocity through the pore throat (U_t) is given as $U_t = Q/2L_t = 42 \text{ mm/s}$. These parametric values of fluid lead to $Wi \approx 10\text{--}47$. The Deborah number ($De = \lambda U_t/l_s$) can also be defined for 2-throats and 10-pores channels. De ranges from 0.05–1.3 for 2-throats channels and 0.42–10.5 for 10-pores channels in the present study. The polymer chains do not have sufficient time to relax before reaching to the next pore in 10 closely placed pores as $De > 1$ for cases with $Wi > 18$ and hence the interactions among the pores are expected. The effect of inertia in our study is negligible as Re is very small, $Re \sim 10^{-5}$. The elasticity number, $El = Wi/Re \sim 10^6$, can be defined to characterise the relative importance of elasticity and inertia. In the present study, the elastic forces dominate over the inertia as $El(\sim 10^6)$ is very large. Therefore, the effect of the change in elastic modulus of fluid due to

the change in λ does not have any significant effect on the results. We use t_{pv} as the characteristic timescale in the present study. $t_{pv} = 0.07$ s is constant due to the fixed flow rate. We performed simulations for dimensional time $t_{max}^* = 1.0$ s, which corresponds to $t_{max} = t_{max}^*/t_{pv} \approx 14$ and varies from $t_{max}^*/\lambda = 50$ at $Wi = 10$ to $t_{max}^*/\lambda = 2$ at $Wi = 47$. t^* is dimensional time and $t = t^*/t_{pv}$ is dimensionless time. The flow converges to steady state for $t > 0.2$ at $Wi = 0.3$ (almost Newtonian fluid) and for fluctuating flows instability becomes fully developed for $t > 1$ (see the Appendix). We use time interval $t = 2-14$ to calculate the statistics. Here, the maximum simulation time ($t_{max} \approx 14$) is sufficient for the convergence of the statistics. We use $1/t_{pv}$ to scale the frequency and viscous stress $\eta U_t/L_t$ to normalize polymeric stresses and pressure. In the next section, we study the flow field and elastic-induced instability in the above mentioned geometry (Fig. 1) for three different cases: a single-pore throat (Sec. IV A), two widely separated pore throats (Sec. IV B) and ten closely spaced pores (Sec. IV C).

IV. RESULTS AND DISCUSSION

A. Single-pore throat

To investigate the polymeric flow instability in the porous media, we start our study with a relatively simple geometry. Therefore, first we consider a channel with a single-pore throat and study the dynamics of polymeric fluid flow in the channel. Eddies appear upstream of the throat (Supplemental Material, video 1) [102]. At $Wi < Wi_{cr}$ these eddies form in both top and bottom regions. However, above a threshold Wi strong spatial and temporal fluctuations in flow velocity occur, leading to fluctuations in the position of eddies. Fluctuations are largely suppressed downstream of the pore throat, and eddy formation is weak [46,47]. We can link these flow features to underlying polymer conformations by computing the polymeric stress tensor [Fig. 2(a)]. The trace of polymeric stress tensor [$\text{tr}(\tau_p)$] physically represents the elongation of the polymeric chains in the solution, where the higher value of trace corresponds to the larger stretching of the chains. In the high stress regions polymer chains are highly stretched, obstructing the fluid flow crossing the high stress regions and facilitating the flow separation (i.e., formation of eddies). In the upstream, the streak of large $\text{tr}(\tau_p)$ are detached from the wall and goes into the middle of the constriction, indicating high polymer elongation, which drives eddy formation upstream of the constriction. The low value of $\text{tr}(\tau_p)$ within the upstream eddy indicates that eddy formation reduces polymer stress [Fig. 2(a)]. Polymeric chains inside the channel in the downstream of the throat are relaxed as the high polymeric stress regions occur close to the walls [Fig. 2(a)], which facilitates the divergence of the flow inside the channel and makes downstream region eddy free. Downstream of the constriction there appear to be waves of higher polymer extension being advected further downstream. To quantify the length of eddies (L_{eddy}) upstream of the throat, we plot x -component of velocity (U_x) at a distance $\Delta y/W = 0.015$ (Δy is the height of first grid element next to the wall) away from the wall [Fig. 2(b)]. L_{eddy} is the length measured from the first stagnation point (left most of the throat) to the start of the throat (i.e., $x = 0$). Thus, L_{eddy} covers all the upstream eddies shown in Fig. 2(a). If eddies appear on both top and bottom regions, $L_{eddy} = \max(L_{eddy}^{top}, L_{eddy}^{bottom})$. We have plotted L_{eddy} in the upstream of the pore throat at different Wi [Fig. 2(c)]. The instantaneous length of eddies fluctuates with time. However, the time-averaged length of eddies along with the intensity of fluctuations increases as Wi increases [Fig. 2(c)]. These findings are consistent with the experimental observations [43,45,47,48,50–53,68,83,103–106].

The power spectral density (PSD) of the normalized instantaneous eddy length depicts the strength of variations of L_{eddy} at different frequencies [Fig. 2(d)]. The dimensionless frequency spectrum of the fluctuation of L_{eddy} is in the range of 0–9 [Fig. 2(d)]. The PSD of smaller frequencies is larger than that of higher frequencies. The PSD of larger frequencies increases with Wi , which shows the increase of temporal fluctuations of L_{eddy} with Wi . We also study the statistics of L_{eddy} at different Wi in a single throated channel [Fig. 3(a) and 3(b)]. The probability distribution of eddies' length (L_{eddy}) shows that the range of L_{eddy} increases with Wi [Fig. 3(a)]. We have plotted the mean

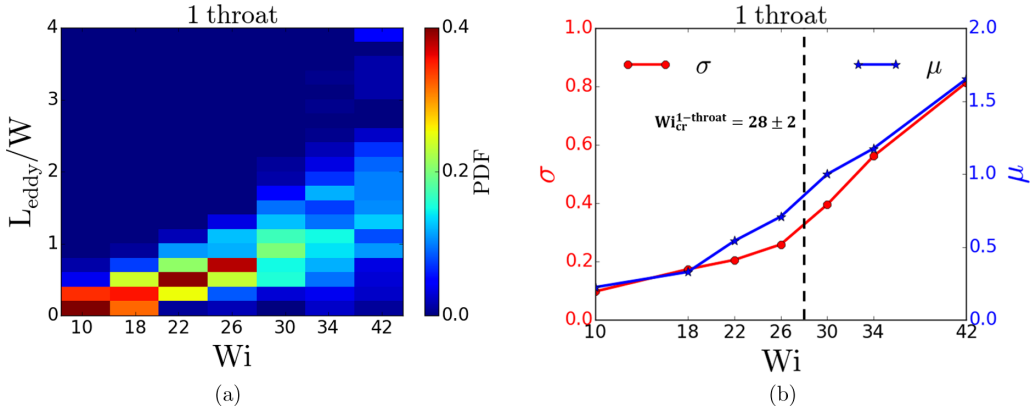


FIG. 3. (a) Probability density function of dimensionless eddy length (L_{eddy}/W) in a single throated channel. (b) Mean (μ) and standard deviation (σ) of normalized eddies' length.

(μ) and standard deviation (σ) of normalized eddies' length (L_{eddy}/W) to further quantify the range of eddies' length [Fig. 3(b)]. The standard deviation monotonically increases with Wi ; however, the slope of σ changes between $Wi = 26$ – 30 . Therefore, we define $Wi_{\text{cr}} = 28 \pm 2$ as the onset of instability in a single throated channel. Figure 3(b) also shows that the mean (μ) of L_{eddy} increases with Wi . Wi_{cr} based on the change in the slope of σ is simply a choice made that does not influence any of the interpretations, and a different choice made by defining Wi_{cr} as the change in the slope of μ gives similar Wi_{cr} values.

B. Two widely separated pore throats

After analyzing the flow dynamics in a channel with a single-pore throat, we consider a channel with two widely separated pore throats ($l_s = 8W$) (Supplemental Material, video 2) [102]. The eddies in front of each throat are unstable and the strength of fluctuations increases with Wi [Fig. 4]. Similar to the single throat channel, the detachment of a streak of large $\text{tr}(\tau_p)$ from the wall leads to eddy formation in the upstream of each throat, whereas high $\text{tr}(\tau_p)$ close to the wall corresponds to eddy-free region downstream of the throat [Fig. 5(a)]. We also observe the waves of higher polymer extension being advected further downstream of each throat. We do not find any strong correlation between the length of eddies in the upstream of pore throats [Fig. 5(b)]. However, we note that the time-averaged length of eddies upstream of first pore throat is slightly larger than that of the second pore throat [Fig. 4]. To quantify instantaneous correlation between L_{eddy} of first and second throat,

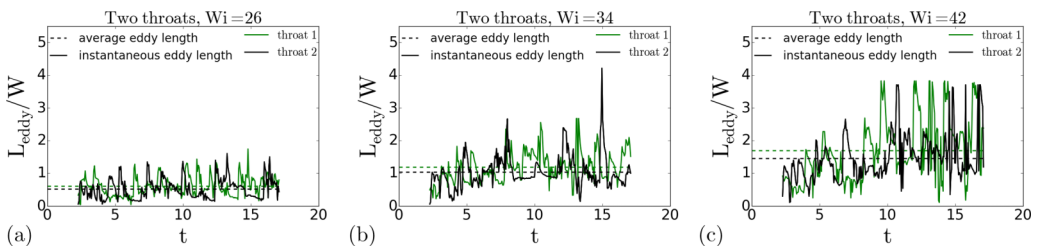


FIG. 4. The instantaneous and time-averaged length of eddies in the upstream of throat-1 and throat-2 at different Wi of a double throated channel. Time is normalized with volumetric flow timescale t_{pv} .

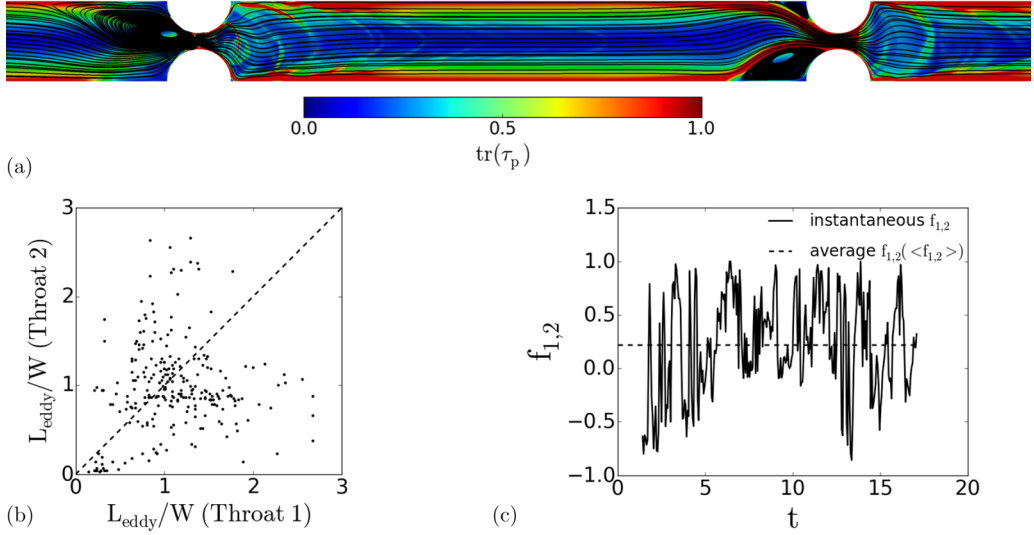


FIG. 5. (a) Streamlines and trace of polymeric stress tensor in a channel with two throats at $Wi = 34$. (b) The correlation between instantaneous eddy lengths of throat-1 and throat-2 at $Wi = 34$ in a channel of two pore throats. (c) Instantaneous $f_{1,2}$ and time-average $\langle f_{1,2} \rangle$ value of the correlation function between the eddy of throat 1 and throat 2 at $Wi = 34$.

we define a correlation function $f_{1,2}$ as:

$$f_{1,2} = 1 - \frac{2|(L_{\text{eddy}})_1 - (L_{\text{eddy}})_2|}{\max((L_{\text{eddy}})_1, (L_{\text{eddy}})_2)}, \quad (7)$$

where $f_{1,2} \rightarrow 1$ corresponds to similar eddies upstream of both throats, whereas $f_{1,2} \rightarrow -1$ implies maximum difference between the length of eddies [Fig. 5(c)]. The polymeric stress relaxation downstream of the first throat (except in the region very close to the wall, where the polymer is strongly stretched) can hinder the eddy formation upstream of the second throat [Fig. 5(a)]. Due to large separation between the throats ($De < 1$), the effect of the first throat on the eddy formation upstream of the second throat is small. This encourages the study of closely located throats ($De > 1$), where high polymeric stress regions formed by one throat can easily interact with that of neighboring throat. As Wi is increased, the enhanced stretching of polymers leads to the formation of longer eddies. The difference between the average length of eddies upstream of first and second throats also increases with Wi [Fig. 4], because the relaxed polymeric stress region downstream of first throat has stronger impact on the eddies upstream of second throat as Wi increases.

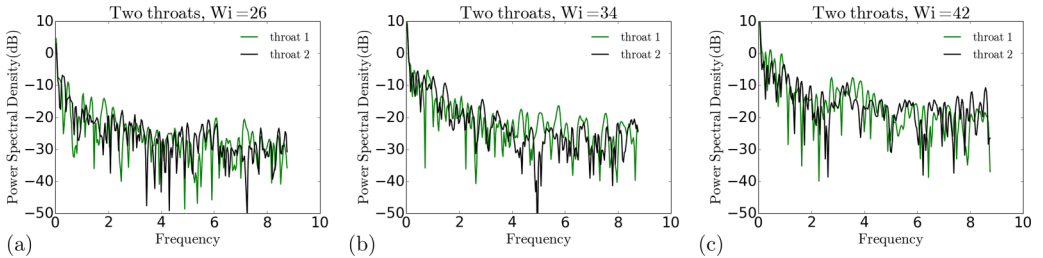


FIG. 6. Power spectral density of normalized eddies' length (L_{eddy}/W) at (a) $Wi = 26$, (b) $Wi = 34$, and (c) $Wi = 42$.

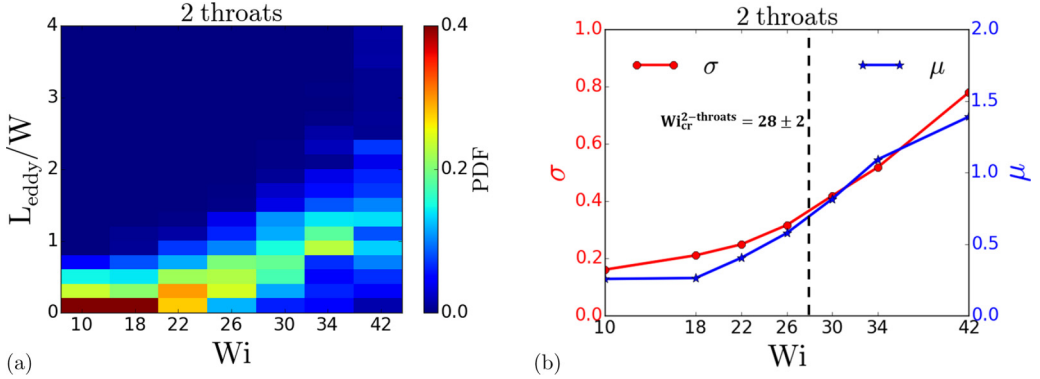


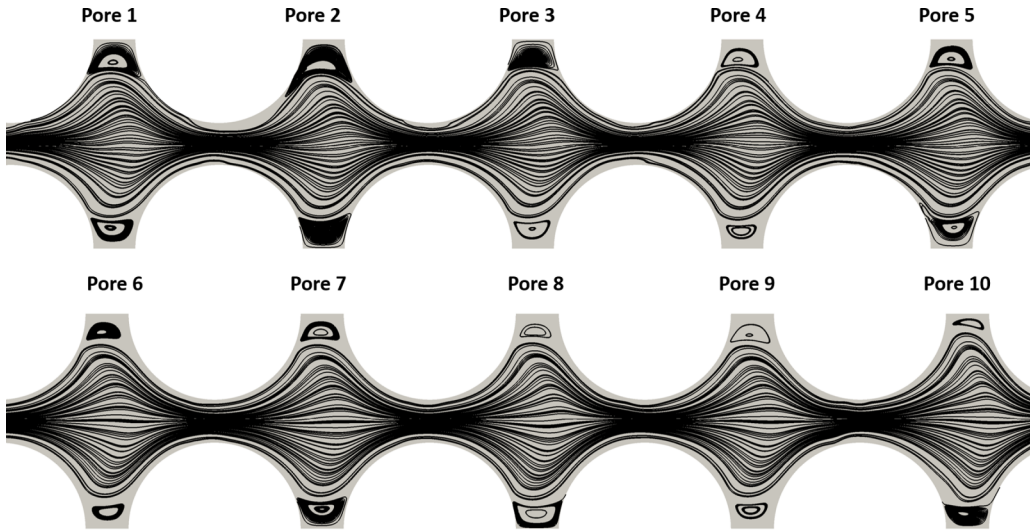
FIG. 7. (a) Probability density function of dimensionless eddy length in two widely separated throats channel. (b) Mean (μ) and standard deviation (σ) of normalized eddies' length.

We have also plotted the power spectral density of the normalized eddy length in Fig. 6 to visualize the fluctuations frequency spectrum. Similar to the single throated channel, the PSD of L_{eddy} in the double-throated channel also increases with Wi , which corresponds to an increase in the fluctuations of L_{eddy} with Wi . Figure 7(a) depicts the probability density function (PDF) of eddies' length in the channel of two widely separated throats. We quantify the standard deviation (σ) and mean (μ) of L_{eddy} in Fig. 7(b). Both, σ and μ increase with Wi . We consider $Wi_{\text{cr}} = 28 \pm 2$ as the threshold of the instability as the slope of σ changes between $Wi = 26$ – 30 .

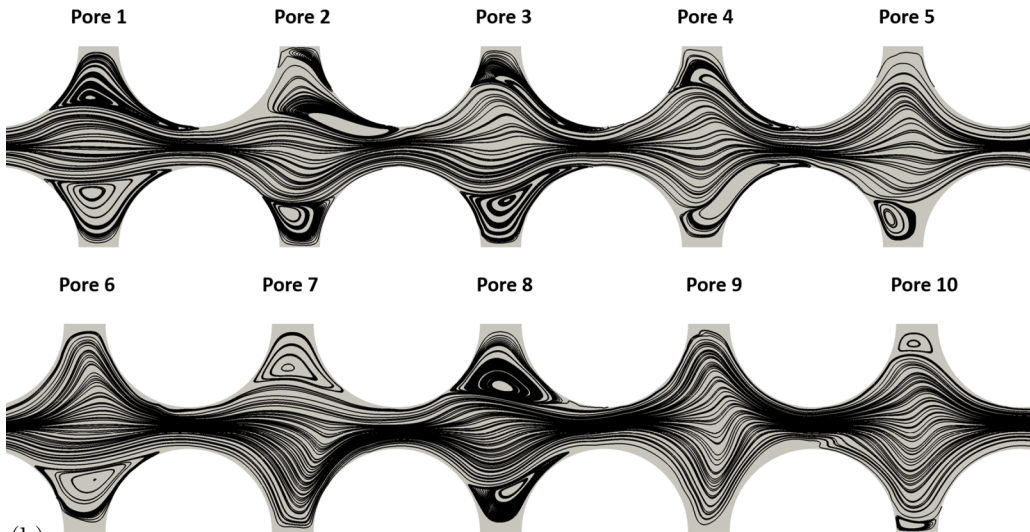
C. Ten closely located pores

The study of single and double throated channels reveal the eddy formation on the upstream of the throat and the eddy-free region downstream of the throat. These two contradictory behaviors compete in the region enclosed between closely located throats (i.e., pores) and determine the flow pattern inside the pore. Here, we study the dynamics of flow of the polymeric fluid inside 10 identical closely ($l_s = W$) interconnected pores (Fig. 1). For a Newtonian fluid, stable eddies appear on the top and bottom of each pore (Appendix). At $Wi < Wi_{\text{cr}}$, the flow of polymeric fluid inside the pores forms eddies on the top and bottom of each pore (see Supplemental Material, video 3) [102], whereas at $Wi > Wi_{\text{cr}}$, the eddy on the top as well as bottom of the pores collapse and reform (Supplemental Material, video 4) [102]. At $Wi = 18 (< Wi_{\text{cr}})$, all the pores in the channel have a similar eddy pattern [Fig. 8(a)]. Figure 8(b) depicts the snapshot of streamlines across the pores at $Wi = 34 (> Wi_{\text{cr}})$. The pattern of polymeric fluid flow inside the pore at $Wi = 34$ can be divided into 4 distinct types [Fig. 8(b)]: (1) eddies on both top and bottom regions of pore (i.e., pore 8), (2) eddy-free bottom region of pore (i.e., pore 7), (3) eddy-free pore (i.e., pore 9), and (4) eddy-free top region of pore (i.e., pore 6). These patterns are unstable and interchange frequently (Supplemental Material, video 4) [102]. Often the size of eddies at $Wi > Wi_{\text{cr}}$, when the eddies appear on both top and bottom of the pore (pore type 1), is different (i.e., pore 2). These coherent flow structures (i.e., multistability) [Fig. 8(b)], that are persistent in time despite the underlying unstable flow, have been also reported in experiments [47].

The flow structure in each pore is closely coupled to the underlying polymeric stress field, which controls the local rheology. For the flow at $Wi = 18 < Wi_{\text{cr}}$, the two regions of high polymeric stress in the top and bottom of the pore correspond to the regions where the flow separated from the wall to form eddies [Figs. 8(a) and 9(a)]. The polymer stress profile is similar among the pores at $Wi < Wi_{\text{cr}}$ ($Wi = 18$), therefore we see a similar flow pattern in different pores. At $Wi > Wi_{\text{cr}}$, both the polymeric stress field and the velocity field are unstable and vary between pores [Figs. 8(b) and 9(b)]. The multistability of the flow pattern inside the pores at $Wi = 34$ [Fig. 8(b)] can be



(a)



(b)

FIG. 8. (a) Instantaneous streamlines in a channel of 10 closely interconnected pores at $Wi = 18$ and dimensionless time, $t \approx 6$. (b) Instantaneous streamlines in a channel of 10 closely interconnected pores at $Wi = 34$ and dimensionless time, $t \approx 10$.

explained with the help of corresponding high polymeric stress regions shown in Fig. 9(b). There are two high stress regions in the middle of the eighth pore, which coincide with the formation of eddies on the top and the bottom of the pore. Everywhere inside the ninth pore, the polymeric chains are unstretched (i.e., the high stress regions only occur close to the walls), and hence the flow diverges in this pore and we do not see any eddy. High polymeric stress occurs in the top region of the seventh pore, therefore an eddy appears only in the top region of the pore and the bottom region is eddy free. Conversely, there is a high stress region in the bottom region of the sixth pore, and therefore the eddy forms only in the bottom region of the pore. Thus, the stretched polymeric chains inside the pore lead to eddy formation, while coiled chains lead to

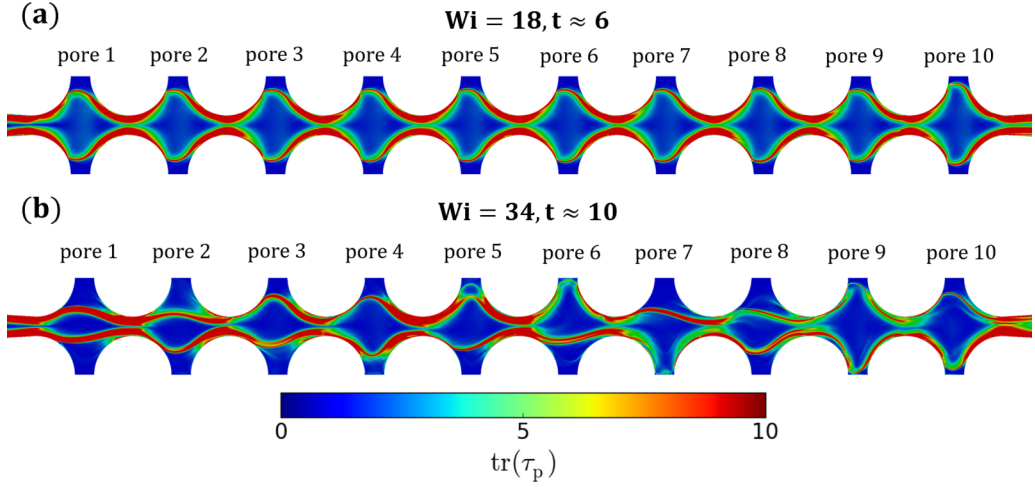


FIG. 9. The snapshot of the trace of polymeric stress tensor at (a) $Wi = 18, t \approx 6$ and (b) $Wi = 34, t \approx 10$. These plots of trace of polymeric stress correspond to the streamlines shown in Figs. 8(a) and 8(b), respectively.

eddy-free regions. This explanation also holds for the other pores in Fig. 8(b). Similarly, a streak of high stress has been observed in the wake of a confined cylinder in a complex fluid [75,84]. The asymmetric flows of polymeric fluids in cross-slot geometries also exhibit streaks of high stress [107–110].

Now, we study the time dependent behavior of an individual pore. We quantify the area occupied by eddies on the top and bottom regions of the second pore separately [Fig. 10(a)]. At $Wi < Wi_{cr}$, we always observe eddies on both the top and bottom regions of the pore [Fig. 10(a)]. Whereas, the size of both eddies is constant at $Wi = 0.3$ (Appendix). To visualize the time dependent behavior of high polymeric stress regions, we plot the contours of trace of polymeric stress tensor across the channel at the center of the second pore [i.e., along the red line shown in the inset of Fig. 10(a)] in Fig. 10(b). The peak value of the trace of polymer stress tensor corresponds to the flow-separation region (i.e., the distance from the wall of the channel, where streamlines separate from the main flow and form a closed streamline to make eddies). The contour of the trace of polymer stress also has two distinct regions well inside the pore where the maximum value of polymer stress tensor occurs, which further supports the presence of two distinct regions where flow separation takes place [Fig. 10(b)].

The flow pattern inside the pore is transient at $Wi > Wi_{cr}$ and each pore can exhibit all 4 kinds of flow patterns discussed earlier. The area of eddies, whether it is in the top region or bottom region of the pore, fluctuates [Fig. 10(c)]. The transition from one flow pattern to another can be easily seen in Fig. 10(c). There are eddies on the top as well as bottom regions of the pore in the beginning of the simulation (flow pattern type 1), but the area of eddies is not identically equal and the difference between the area of eddies increases with time. Eventually, the eddy in the bottom of the pore completely disappears and a new flow state with an eddy only on the top region of the pore (type 2) emerges. Next, both eddies disappear and the pore becomes completely eddy free (type 3). Finally, the eddy in the bottom region of the pore again reappears and it leads to the formation of a different flow state inside the pore, where the top region of the pore is eddy free and bottom region has eddy (type 4). Thus, the flow patterns of the polymeric fluid inside the pore are transient. Other pores in the channel also exhibit similar transitions, though the switching between flow states does not show any clear pattern. As $Wi (> Wi_{cr})$ increases, the distinct flow structures change even more frequently.

The time dependent flow patterns inside the pore at $Wi > Wi_{cr}$ [Fig. 10(c)] can be explained using the trace of polymeric stress tensor across the channel at the center of the pore [Fig. 10(d)]. Part I

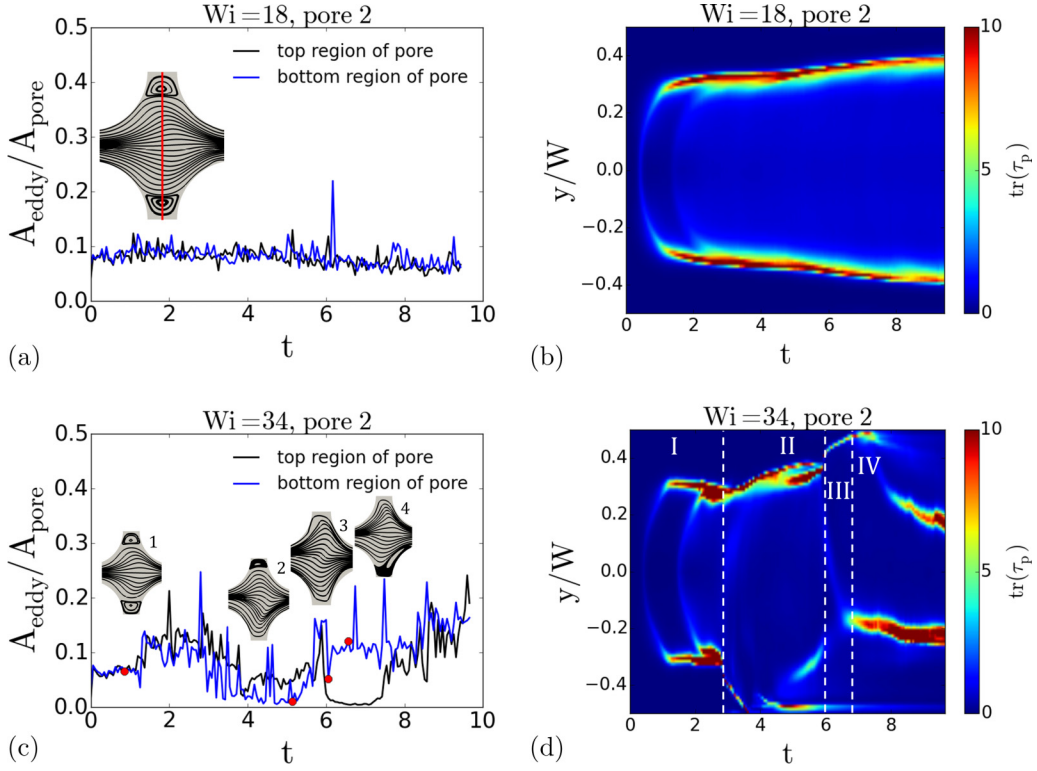


FIG. 10. (a) The ratio of eddy to pore area for “pore 2” as a function of time at $Wi = 18$. A_{eddy} is the area of eddies in a particular half region of the pore, while A_{pore} is the total area of the pore. The streamlines inside the pore represent the flow pattern at the center of the pore [i.e., along the red line shown in the inset of Fig. 10(a)]. (b) The contour of the trace of polymeric stress tensor across the channel at the center of the pore [i.e., along the red line shown in the inset of Fig. 10(a)]. (c) The ratio of eddy to pore area for “pore 2” as a function of time at $Wi = 34$. The snapshots of streamlines inside the pore represent the flow pattern at specific time indicated by red solid circles. (d) The contour of the trace of the polymer stress tensor across the channel at the center of the pore. The upper limit of time in these plots ($t = 9.5$) corresponds to $t^*/\lambda = 13.4$ for $Wi = 18$ and $t^*/\lambda = 3.3$ for $Wi = 34$.

of Fig. 10(d) depicts that there are two distinct regions, approximately equidistant from the walls, where maximum values of the trace of polymer stress occur. This distribution of stress corresponds to a pattern where both top and bottom regions of the pore have eddies [pore type 1 in Fig. 10(c)]. Part II has a single region inside the pore with peak value of trace of polymer stress and it lies on the top region of the pore. The local peak value of trace of polymer stress in the bottom region of the pore lies close to the wall and is much smaller than the global maximum. This stress distribution represents the pattern where top region of the pore has an eddy and bottom region of the pore is eddy free [type 2 in Fig. 10(c)]. In part III, the streaks of peak $\text{tr}(\tau_p)$ in both top and bottom regions of the pore are close to the walls and their peak values are much smaller than the global maximum of $\text{tr}(\tau_p)$ [Fig. 10(d)]. In this case, the pore exhibits an eddy-free flow state [type 3 in Fig. 10(c)]. Part IV also has a single region where maximum value of trace of polymer stress occurs, but it lies on the bottom region of the pore. This stress distribution leads to the pattern where bottom region of the pore has an eddy and the top region of the pore is eddy free [type 4 in Fig. 10(c)]. Figure 10(d) also shows that the eddy-free flow state (type 3) exists for a shorter time compared to other flow states.

We study the correlation between the area of eddies for different pairs of pores. To quantify the correlation between the area of eddies of two pores, we modify the correlation function [Eq. (7)]

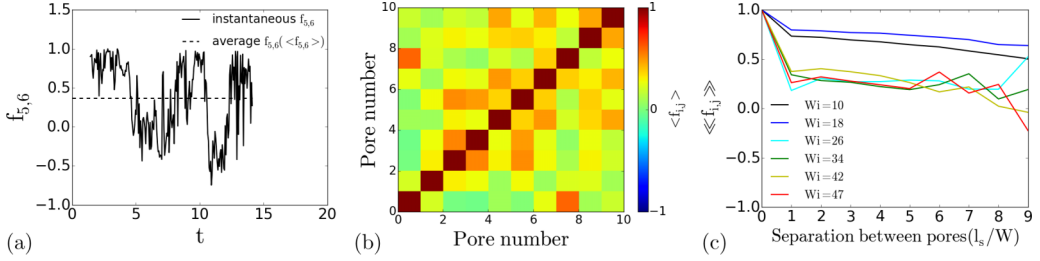


FIG. 11. (a) Instantaneous $f_{5,6}$ and time-average $\langle f_{5,6} \rangle$ values of the correlation function between pore 5 and pore 6 at $Wi = 34$. (b) The time average value of correlation function for different pairs of the pores at $Wi = 34$. (c) The value of $\langle f_{i,j} \rangle$, further averaged across the pores of the same separation, as a function of pore separation at different Wi .

$f_{i,j}$ as

$$f_{i,j} = 1 - \frac{2|(A_{\text{eddy}}/A_{\text{pore}})_i - (A_{\text{eddy}}/A_{\text{pore}})_j|}{\max[(A_{\text{eddy}}/A_{\text{pore}})_i, (A_{\text{eddy}}/A_{\text{pore}})_j]} \quad (8)$$

The value of correlation function $f_{i,j}$ varies from +1 in the case where both the pores have similar eddy pattern to -1 in the case where one pore has an eddy and the other is eddy free. The value of $f_{i,j}$ varies with time for any given pair of pores, which indicates the transient nature of the correlation between the pores [Fig. 11(a)]. Therefore, the pattern of eddies inside the pores exhibits both positive and negative correlations. We use the time average of $f_{i,j}$ ($\langle f_{i,j} \rangle$) to study the statistics of the correlations between the eddies of two pores in a long time. Figure 11(b) depicts the time average value of $f_{i,j}$ for different pairs of pores at $Wi = 34$. There is a relatively stronger positive correlation between the eddies' area of the nearby pores and the correlation weakens as the separation between the pores increases. Conversely, we also notice a relatively weak correlation between pore-8 and pore-9 ($\langle f_{8,9} \rangle = 0.17$) and relatively strong correlation between pore-1 and pore-8 ($\langle f_{1,8} \rangle = 0.6$) at $Wi = 34$ [Fig. 11(b)]. To further investigate the effect of Wi and the pores' separation on the correlation, we plot $\langle\langle f_{i,j} \rangle\rangle$ as the function of pore separation at different Wi , where $\langle\langle f_{i,j} \rangle\rangle$ is the value of $\langle f_{i,j} \rangle$ averaged across the pores of the same separation [Fig. 11(c)]. At $Wi < Wi_{\text{cr}}$, the correlation between the flow patterns inside the pores is stronger compare to $Wi > Wi_{\text{cr}}$ and $\langle\langle f_{i,j} \rangle\rangle$ monotonically decreases as the separation between the pores increases. For $Wi > Wi_{\text{cr}}$, irrespective of separation between the pores, the correlation is weak (i.e., $\langle\langle f_{i,j} \rangle\rangle < 0.5$) [Fig. 11(c)].

We have also plotted the probability distribution of the area occupied by eddies inside each individual pore in the channel of 10 closely located pores at different Wi [Fig. 12(a)]. The value of $A_{\text{eddy}}/A_{\text{pore}}$ ranges 0.1–0.25 at $Wi = 18$, whereas it varies from 0.0 (eddy-free pattern) to 0.5 at $Wi = 47$. The eddy does not disappear in either regions of the pore at $Wi < Wi_{\text{cr}}$, while often it disappears at $Wi > Wi_{\text{cr}}$. Thus, the area of eddies and flow pattern inside the pores are highly predictable for $Wi < Wi_{\text{cr}}$, but not at $Wi > Wi_{\text{cr}}$. We have calculated the standard deviation (σ) and mean (μ) of $A_{\text{eddy}}/A_{\text{pore}}$ in Fig. 12(b) to quantify the fluctuation of eddies' area. The standard deviation of eddies' area increases with Wi for $Wi > Wi_{\text{cr}}$ and the onset of the increase of σ lies between $Wi = 18$ –22. Therefore, we consider $Wi_{\text{cr}} = 20 \pm 2$ as the critical Wi of the multistability. The threshold Wi , above which multistability appears, for the channel of 10 closely located pores ($Wi_{\text{cr}} = 20 \pm 2$) [Fig. 12(b)] is smaller than the channel with single or two widely separated throats ($Wi_{\text{cr}} = 28 \pm 2$) [Figs. 3(b) and 7(b)]. When the pores are closer to each other, the onset of multistability arises at lower Wi , due to the advection of polymer stress between the pores. Similar observation was reported in experiments [47]. We have also noticed that sometime eddies appear even at the center of the pore with/without eddies on the top or bottom region of the pore at $Wi > Wi_{\text{cr}}$ [Fig. 13]. This behavior has not been reported in prior experimental studies.

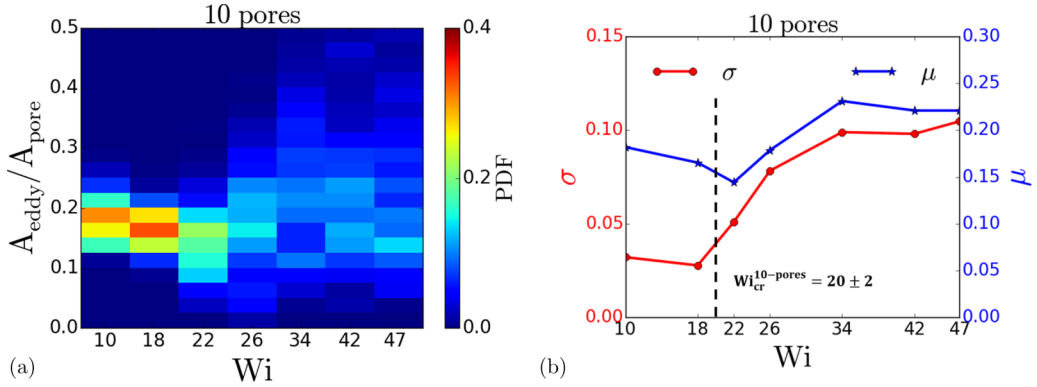


FIG. 12. (a) PDF of the ratio of eddies to pore area ($A_{\text{eddy}}/A_{\text{pore}}$) at different Wi for a channel of 10 closely located pores. A_{eddy} represents total area occupied by eddies in an individual pore and A_{pore} is the total area of the pore. Above a threshold Wi , there appears to be multistability, and the eddy areas take on a broad range of values. (b) Mean (μ) and standard deviation (σ) of normalized eddies' area.

The pressure drop of the flow inside the porous media is an important macroscopic property due to practical application in the field of oil recovery [6] and ground water remediation [7,8]. To understand the spatial distribution of pressure, we have plotted the contours of dimensionless pressure (p) in Fig. 14(a) for the flow field shown in Fig. 8(b) (i.e., $Wi = 34$, $t \approx 10$). We have also plotted the pressure profile along the centerline of the channel [i.e., red solid line in Fig. 14(a)] [Fig. 14(b)] and at the center of the pore along the width [i.e., dashed yellow line in Fig. 14(a)] [Fig. 14(c)]. The pressure inside the channel does not decrease monotonically due to the converging-diverging geometry of the channel [Fig. 14(b)]. For the cross-section at the center of an individual pore, the pressure is maximum at the centerline (i.e., $y = 0$) of the channel [Fig. 14(c)]. Instantaneous pressure drop across the channel along the centerline [Δp in Fig. 14(a)] is transient due to instability and the fluctuation intensifies as Wi increases [Fig. 15(a)]. We calculate the time averaged pressure drop ($\langle \Delta p \rangle$) along with fluctuations across the channel for a fixed volumetric flow rate at different Wi [Fig. 15(b)]. The instability inside the pores facilitates the flow and lowers the hydrodynamic

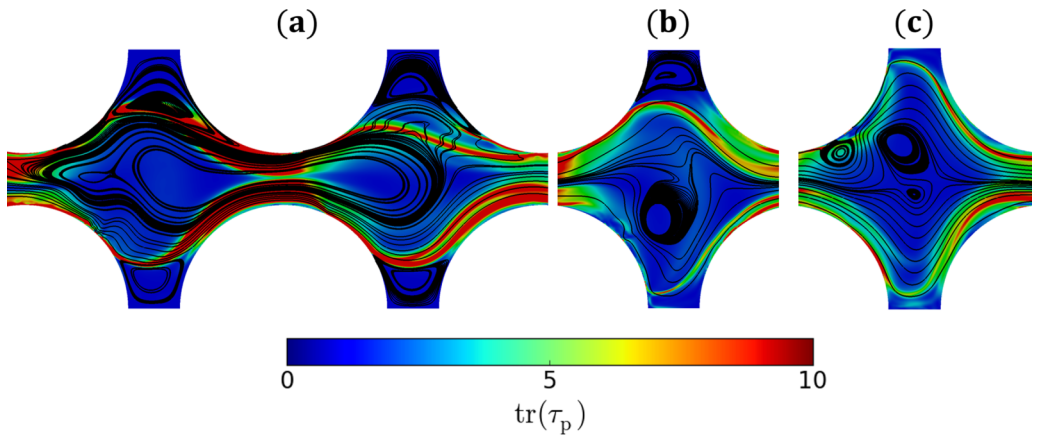
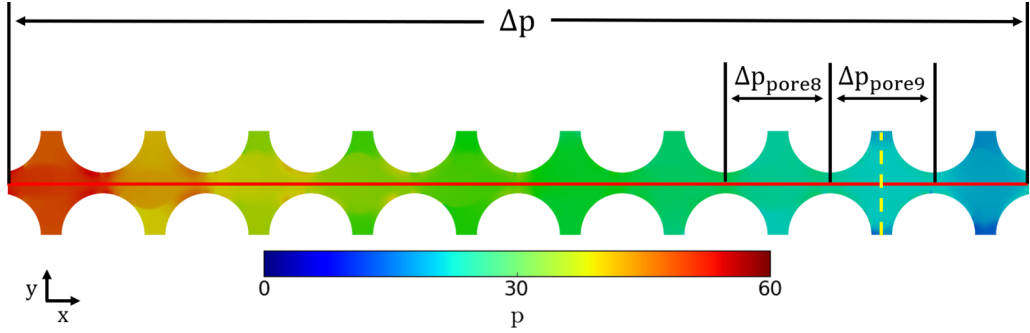
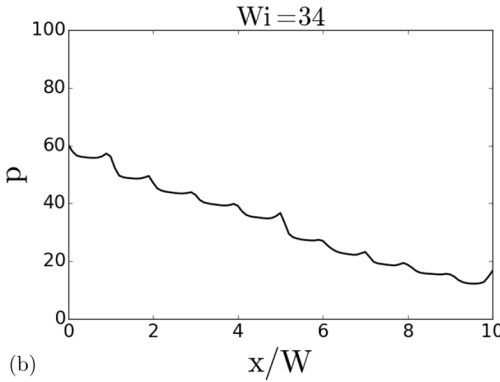


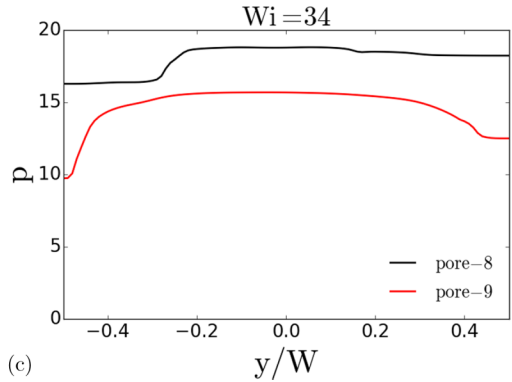
FIG. 13. Eddies at the center of the pore at $Wi = 34$. (a) Eddy at the center as well as the top and bottom regions of the pore. Here, the eddy at the center persists in two pores. (b) Eddies at the center and the top region of the pore, while bottom region is eddy free. (c) Eddies only at the center of the pore. Top and bottom regions are eddy free.



(a)



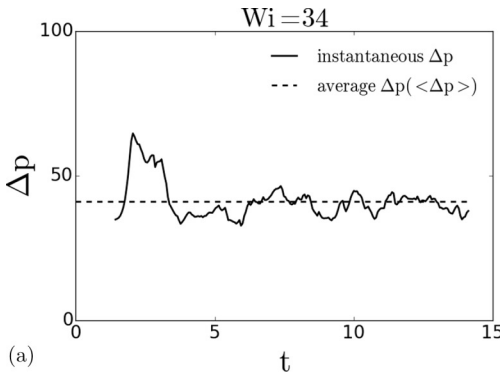
(b)



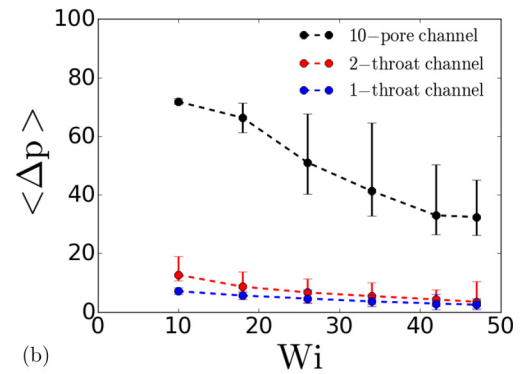
(c)

FIG. 14. Dimensionless pressure for the flow field shown in Fig. 8(b) (i.e., $Wi = 34$, $t \approx 10$): (a) The contours of pressure field inside the channel. (b) Pressure along the centerline of the channel [i.e., red solid line in Fig. 14(a)]. (c) Pressure across the channel at the center of the pore [i.e., dashed yellow line in Fig. 14(a)].

drag, which leads to a smaller pressure drop across the channel as Wi increases [Fig. 15(b)]. To further understand the mechanism of hydrodynamic drag reduction with increasing Wi , we calculate the pressure drop across individual pores along the centerline of the channel [specially, pore-8 and pore-9 as depicted in Fig. 14(a)] for the flow state shown in Fig. 8(b). The pressure drop across an eddy-free pore is smaller than the pressure drop across the pore with eddies [Example:



(a)



(b)

FIG. 15. (a) Instantaneous and time averaged pressure drop across the channel of 10 pores at $Wi = 34$. (b) Averaged pressure drop ($\langle \Delta p \rangle$) across the channels at different Wi .

$\Delta p_{\text{pore-9}} = 3.45$ for pore-9 shown in Fig. 8(b) and $\Delta p_{\text{pore-8}} = 4.6$ for pore-8 shown in Fig. 8(b)]. Because, the eddy-free pore has larger apparent width involve in the net volumetric flow (i.e., fluid circulates inside an eddy and does not contribute in any net volumetric flow) and the pressure drop in the channel is inversely related to its apparent width. The presence of eddy-free pores at $Wi > Wi_{cr}$ leads to smaller pressure drop across the channel, in contrast with a channel at $Wi < Wi_{cr}$ where all the pores have eddies. We have also calculated the pressure drop in single and double throated channels for the length same as the channel of 10 pores. The pressure drop in the single as well as double throated channel is much smaller due to lesser constriction and it also decreases with Wi due to instability [Fig. 15(b)].

V. CONCLUSIONS

The addition of polymers and surfactants to the displacing fluid is essential to the ground water remediation and enhance oil recovery for addressing rapidly growing demand of water and energy [111–115]. We numerically study the flow of a polymeric fluid in channels consisting of converging and diverging physical constraints. We use channels with a single-pore throat, two widely separated pore throats and ten closely separated pores to study an elastic-induced flow instability at different Wi . The channels with either a single-pore throat or two widely separated pore throats have unstable eddies in the upstream of the pore throats whose average length (L_{eddy}) increases with Wi . In the case of 10 closely placed pores, eddies appear on both top and bottom regions of the pores at $Wi < Wi_{cr}$, whereas the flow exhibits 4 distinct types of patterns inside the pores at $Wi > Wi_{cr}$. The eddies on both the top and bottom regions of the pores regularly collapse and reform at $Wi > Wi_{cr}$. This behavior of eddies leads to flow patterns where eddies appear in either one region, both regions, or neither region of the pore (eddy free). The high polymeric stress region inside the pore induces eddy formation, whereas the high stress region close to the walls leads to eddy collapse. There is a positive correlation between the eddy areas of neighboring pores in the long-time statistics, but this correlation weakens as the separation between the pores increases. The correlation between the pores also weakens as Wi increases. The eddy-free pores also lead to reduced hydrodynamic drag across the channel at $Wi > Wi_{cr}$. Disorder of the porous media is expected to play a large role in altering the instability, and would be an interesting parameter to consider in a future study [59,82]. The presence of higher connectivity and elevated disorder in 3D porous media [116] should also affect the elastic instability.

ACKNOWLEDGMENTS

A. M. Ardekani acknowledges the financial support from the National Science Foundation (Grants No. CBET-1700961 and No. CBET-1705371). M.K. was supported in part by the Ross graduate fellowship from Purdue College of Engineering. This work used the Extreme Science and Engineering Discovery Environment (XSEDE) [117], which is supported by the National Science Foundation Grant No. ACI-1548562 through allocations TG-CTS180066 and TG-CTS190041 to A.M.A. Acknowledgment is made to the Donors of the American Chemical Society Petroleum Research Fund for partial support of this research to S.S.D. and C.A.B through Grant No. PRF 59026-DNI9. This material is also based upon work supported by the National Science Foundation Graduate Research Fellowship Program (to C.A.B.) under Grant No. DGE1656466. Any opinions, findings, and conclusions or recommendations expressed in this material are those of the authors and do not necessarily reflect the views of the National Science Foundation. C.A.B. was also supported in part by the Mary and Randall Hack Graduate Award of the High Meadows Environmental Institute.

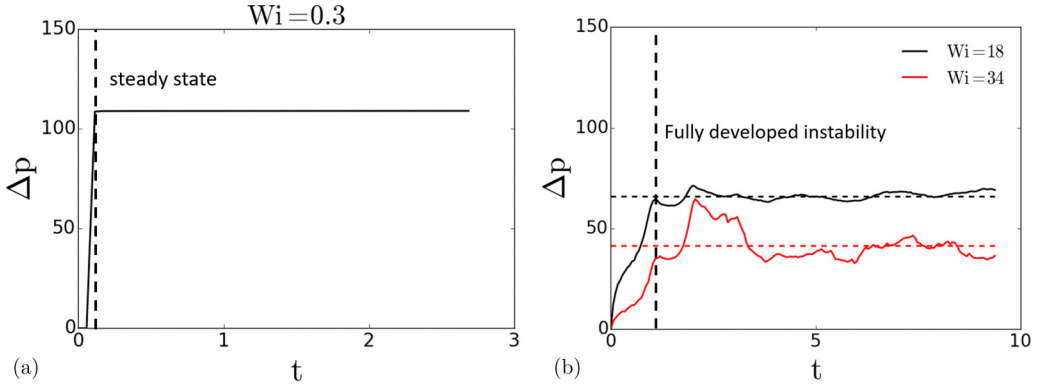


FIG. 16. (a) Dimensionless pressure drop across the channel along the centerline at $Wi = 0.3$ (almost Newtonian fluid). Flow converges to steady state for $t > 0.2$. (b) Dimensionless pressure drop across the channel along the centerline at $Wi = 18, 34$. Fully developed instability occurs for $t > 1$.

APPENDIX

1. Start up transient flow

We use pressure drop (Δp) across the channel along the centerline as a simple metric to characterize the transient start up flow. The flow reaches steady state for $t > 0.2$ at $Wi = 0.3$ (almost Newtonian fluid) [Fig. 16(a)]. For fluctuating flows, the meaning of fully developed flow is that fluctuating quantities have a well-defined mean. The instability becomes fully developed for $t > 1$ as Δp fluctuates around a mean for $t > 1$ [Fig. 16(b)].

2. Eddy area at $Wi = 0.3$ (almost Newtonian fluid)

The size of eddies both top and bottom of the pore at $Wi = 0.3$ becomes time independent for $t > 0.2$ [Fig. 17].

3. Flow of nonshear thinning fluid (FENE-CR) inside the pores

We have also performed a simulation for nonshear thinning model (FENE-CR) at relaxation time $\lambda = 0.2$ s, viscosity ratio $\beta = \eta_s/(\eta_s + \eta_p) = 0.01$, $L^2 = 625$, and volumetric flow rate per unit depth of the channel $Q = 16.8$ mm²/s. These parameters lead to $Wi = 16.4$ for FENE-CR

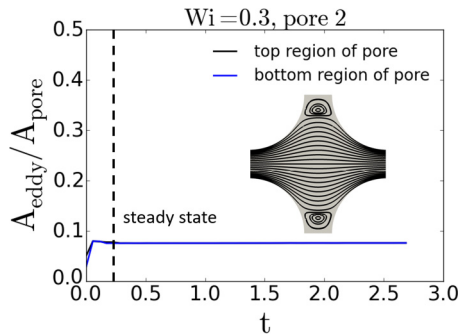


FIG. 17. The area of eddies on the top and bottom of “pore-2” at $Wi = 0.3$.

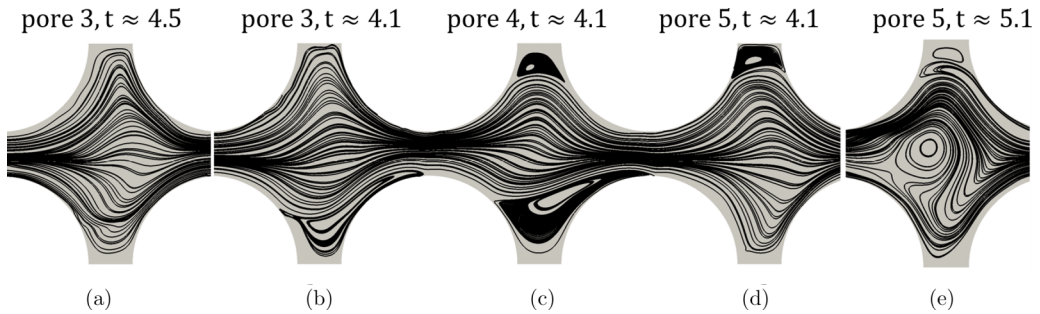


FIG. 18. Instantaneous streamlines in a channel of 10 closely interconnected pores at $Wi = 16.4$ for FENE-CR constitutive model.

model [118]. This model also exhibits multistability similar to FENE-P model (Fig. 18). Figure 18(a) shows eddy-free flow state. Figure 18(b) has eddy only on the bottom region of the pore and top region is eddy free. Figure 18(c) has eddies on both top and bottom region of the pore, whereas Fig. 18(d) represents the flow state where eddy appears only on the top region of the pore and bottom region is eddy free. Nonshear thinning fluid (FENE-CR) also exhibits the flow state wherein the eddy appears at the center of the pore [Fig. 18(e)].

-
- [1] C. A. Browne, A. Shih, and S. S. Datta, Pore-scale flow characterization of polymer solutions in microfluidic porous media, *Small* **16**, 1903944 (2019).
 - [2] C. M. Schroeder, Single polymer dynamics for molecular rheology, *J. Rheol.* **62**, 371 (2018).
 - [3] S. J. Haward, Microfluidic extensional rheometry using stagnation point flow, *Biomicrofluidics* **10**, 043401 (2016).
 - [4] J. R. A. Pearson, Instability in non-Newtonian flow, *Annu. Rev. Fluid Mech.* **8**, 163 (1976).
 - [5] R. G. Larson, Flow-induced mixing, demixing, and phase transitions in polymeric fluids, *Rheol. Acta* **31**, 497 (1992).
 - [6] K. S. Sorbie, *Polymer-improved Oil Recovery* (Springer Science & Business Media, Berlin, 2013).
 - [7] D. Roote, *Technology Status Report: In Situ Flushing* (Ground Water Remediation Technology Analysis Center, Pittsburgh, PA, 1998); <http://www.gwrtac.org>.
 - [8] M. M. Smith, J. A. Silva, J. Munakata-Marr, and J. E. McCray, Compatibility of polymers and chemical oxidants for enhanced groundwater remediation, *Environ. Sci. Technol.* **42**, 9296 (2008).
 - [9] B. Sandiford *et al.*, Laboratory and field studies of water floods using polymer solutions to increase oil recoveries, *J. Pet. Technol.* **16**, 917 (1964).
 - [10] F. Durst, R. Haas, and B. Kaczmar, Flows of dilute hydrolyzed polyacrylamide solutions in porous media under various solvent conditions, *J. Appl. Polym. Sci.* **26**, 3125 (1981).
 - [11] M. J. Pitts, T. A. Campbell, H. Surkalo, K. Wyatt *et al.*, Polymer flood of the rapdan pool, saskatchewan, canada, *SPE Reservoir Eng.* **10**, 183 (1995).
 - [12] D. Wang, G. Wang, H. Xia *et al.*, Large scale high viscoelastic fluid flooding in the field achieves high recoveries, in *SPE Enhanced Oil Recovery Conference* (Society of Petroleum Engineers, Dallas, TX, 2011).
 - [13] B. Wei, L. Romero-Zerón, and D. Rodrigue, Oil displacement mechanisms of viscoelastic polymers in enhanced oil recovery (eor): A review, *J. Pet. Explor. Prod. Technol.* **4**, 113 (2014).
 - [14] E. Vermolen, M. Van Haasterecht, S. Masalmeh *et al.*, A systematic study of the polymer viscoelastic effect on residual oil saturation by core flooding, in *SPE EOR Conference at Oil and Gas West Asia* (Society of Petroleum Engineers, Dallas, TX, 2014).
 - [15] L. J. Fauci and R. Dillon, Biofluidmechanics of reproduction, *Annu. Rev. Fluid Mech.* **38**, 371 (2006).

- [16] D. J. Smith, E. A. Gaffney, and J. R. Blake, Modelling mucociliary clearance, *Respir. Physiol. Neurobiol.* **163**, 178 (2008).
- [17] M. J. Blunt, *Multiphase flow in Permeable Media: A Pore-scale Perspective* (Cambridge University Press, Cambridge, UK, 2017).
- [18] S. S. Datta, H. Chiang, T. S. Ramakrishnan, and D. A. Weitz, Spatial Fluctuations of Fluid Velocities in Flow Through a Three-Dimensional Porous Medium, *Phys. Rev. Lett.* **111**, 064501 (2013).
- [19] P. K. Kang, P. de Anna, J. P. Nunes, B. Bijeljic, M. J. Blunt, and R. Juanes, Pore-scale intermittent velocity structure underpinning anomalous transport through 3D porous media, *Geophys. Res. Lett.* **41**, 6184 (2014).
- [20] T. Pak, I. B. Butler, S. Geiger, M. I. van Dijke, and K. S. Sorbie, Droplet fragmentation: 3D imaging of a previously unidentified pore-scale process during multiphase flow in porous media, *Proc. Natl. Acad. Sci. USA* **112**, 1947 (2015).
- [21] F. Zami-Pierre, R. de Loubens, M. Quintard, and Y. Davit, Transition in the Flow of Power-Law Fluids Through Isotropic Porous Media, *Phys. Rev. Lett.* **117**, 074502 (2016).
- [22] A. M. Howe, A. Clarke, and D. Giernalczyk, Flow of concentrated viscoelastic polymer solutions in porous media: Effect of mw and concentration on elastic turbulence onset in various geometries, *Soft Matter* **11**, 6419 (2015).
- [23] J. Mitchell, K. Lyons, A. M. Howe, and A. Clarke, Viscoelastic polymer flows and elastic turbulence in three-dimensional porous structures, *Soft Matter* **12**, 460 (2016).
- [24] A. Clarke, A. M. Howe, J. Mitchell, J. Staniland, L. A. Hawkes *et al.*, How viscoelastic-polymer flooding enhances displacement efficiency, *SPE J.* **21**, 675 (2016).
- [25] S. S. Datta, J.-B. Dupin, and D. A. Weitz, Fluid breakup during simultaneous two-phase flow through a three-dimensional porous medium, *Phys. Fluids* **26**, 062004 (2014).
- [26] S. S. Datta, T. Ramakrishnan, and D. A. Weitz, Mobilization of a trapped nonwetting fluid from a three-dimensional porous medium, *Phys. Fluids* **26**, 022002 (2014).
- [27] A. Bourgeat, O. Gipouloux, and E. Marusic-Paloka, Filtration law for polymer flow through porous media, *Multiscale Model. Simul.* **1**, 432 (2003).
- [28] B. G. Compton and J. A. Lewis, 3D-printing of lightweight cellular composites, *Adv. Mater.* **26**, 5930 (2014).
- [29] X. Wang, M. Jiang, Z. Zhou, J. Gou, and D. Hui, 3D printing of polymer matrix composites: A review and prospective, *Composites Part B: Engineering* **110**, 442 (2017).
- [30] G. H. McKinley, P. Pakdel, and A. Öztekin, Rheological and geometric scaling of purely elastic flow instabilities, *J. Non-Newtonian Fluid Mech.* **67**, 19 (1996).
- [31] P. Pakdel and G. H. McKinley, Elastic Instability and Curved Streamlines, *Phys. Rev. Lett.* **77**, 2459 (1996).
- [32] R. G. Larson, E. S. Shaqfeh, and S. J. Muller, A purely elastic instability in Taylor–Couette flow, *J. Fluid Mech.* **218**, 573 (1990).
- [33] S. J. Haward and J. A. Odell, Viscosity enhancement in non-Newtonian flow of dilute polymer solutions through crystallographic porous media, *Rheol. Acta* **42**, 516 (2003).
- [34] J. A. Odell and S. J. Haward, Viscosity enhancement in non-Newtonian flow of dilute aqueous polymer solutions through crystallographic and random porous media, *Rheol. Acta* **45**, 853 (2006).
- [35] C. Huh, G. A. Pope *et al.*, Residual oil saturation from polymer floods: Laboratory measurements and theoretical interpretation, in *SPE Symposium on Improved Oil Recovery* (Society of Petroleum Engineers, Dallas, TX, 2008).
- [36] A. Zaitoun, N. Kohler *et al.*, Two-phase flow through porous media: Effect of an adsorbed polymer layer, in *SPE Annual Technical Conference and Exhibition* (Society of Petroleum Engineers, Dallas, TX, 1988).
- [37] A. Zaitoun, H. Bertin, D. Lasseux *et al.*, Two-phase flow property modifications by polymer adsorption, in *SPE/DOE Improved Oil Recovery Symposium* (Society of Petroleum Engineers, Dallas, TX, 1998).
- [38] G. Chauveteau and M. Moan, The onset of dilatant behavior in noninertial flow of dilute polymer solutions through channels with varying cross-sections, *J. Phys. Lett.* **42**, 201 (1981).

- [39] G. Chauveteau, M. Moan, and A. Magueur, Thickening behavior of dilute polymer solutions in noninertial elongational flows, *J. Non-Newtonian Fluid Mech.* **16**, 315 (1984).
- [40] R. Haas and F. Durst, Viscoelastic flow of dilute polymer solutions in regularly packed beds, *Rheol. Acta* **21**, 566 (1982).
- [41] N. E. Dyakonova, J. A. Odell, Y. V. Brestkin, A. V. Lyulin, and A. E. Saez, Macromolecular strain in periodic models of porous media flows, *J. Non-Newtonian Fluid Mech.* **67**, 285 (1996).
- [42] M. G. Saphiannikova, A. A. Darinskii, and N. E. Dyakonova, Computer simulation of dilute polymer solutions in transient elongational flows, *Macromol. Theory Simul.* **9**, 270 (2000).
- [43] X. Shi, S. Kenney, G. Chapagain, and G. F. Christopher, Mechanisms of onset for moderate mach number instabilities of viscoelastic flows around confined cylinders, *Rheol. Acta* **54**, 805 (2015).
- [44] X. Shi and G. F. Christopher, Growth of viscoelastic instabilities around linear cylinder arrays, *Phys. Fluids* **28**, 124102 (2016).
- [45] A. Varshney and V. Steinberg, Elastic wake instabilities in a creeping flow between two obstacles, *Phys. Rev. Fluids* **2**, 051301(R) (2017).
- [46] B. Qin, P. F. Salipante, S. D. Hudson, and P. E. Arratia, Upstream vortex and elastic wave in the viscoelastic flow around a confined cylinder, *J. Fluid Mech.* **864**, R2-1 (2019).
- [47] C. A. Browne, A. Shih, and S. S. Datta, Bistability in the unstable flow of polymer solutions through pore constriction arrays, *J. Fluid Mech.* **890**, 122 (2020).
- [48] E. M. Ekanem, S. Berg, S. De, A. Fadili, T. Bultreys, M. Rücker, J. Southwick, J. Crawshaw, and P. F. Luckham, Signature of elastic turbulence of viscoelastic fluid flow in a single pore throat, *Phys. Rev. E* **101**, 042605 (2020).
- [49] G. Batchelor, The stress generated in a nondilute suspension of elongated particles by pure straining motion, *J. Fluid Mech.* **46**, 813 (1971).
- [50] D. V. Boger, Viscoelastic flows through contractions, *Annu. Rev. Fluid Mech.* **19**, 157 (1987).
- [51] A. Mongruel and M. Cloitre, Extensional flow of semidilute suspensions of rod-like particles through an orifice, *Phys. Fluids* **7**, 2546 (1995).
- [52] A. Mongruel and M. Cloitre, Axisymmetric orifice flow for measuring the elongational viscosity of semi-rigid polymer solutions, *J. Non-Newtonian Fluid Mech.* **110**, 27 (2003).
- [53] L. Rodd, J. Cooper-White, D. Boger, and G. McKinley, Role of the elasticity number in the entry flow of dilute polymer solutions in micro-fabricated contraction geometries, *J. Non-Newtonian Fluid Mech.* **143**, 170 (2007).
- [54] K. Weissenberg, A continuum theory of rheological phenomena, *Nature* **159**, 310 (1947).
- [55] A. Groisman and V. Steinberg, Elastic turbulence in a polymer solution flow, *Nature* **405**, 53 (2000).
- [56] A. Groisman and V. Steinberg, Efficient mixing at low Reynolds numbers using polymer additives, *Nature* **410**, 905 (2001).
- [57] A. Groisman and V. Steinberg, Elastic turbulence in curvilinear flows of polymer solutions, *New J. Phys.* **6**, 29 (2004).
- [58] R. Poole, The Deborah and Weissenberg numbers, *British Soc. Rheol. Rheol. Bull* **53**, 32 (2012).
- [59] D. M. Walkama, N. Waisbord, and J. S. Guasto, Disorder Suppresses Chaos in Viscoelastic Flows, *Phys. Rev. Lett.* **124**, 164501 (2020).
- [60] B. Qin, P. F. Salipante, S. D. Hudson, and P. E. Arratia, Flow Resistance and Structures in Viscoelastic Channel Flows at Low Reynolds Number, *Phys. Rev. Lett.* **123**, 194501 (2019).
- [61] B. Qin and P. E. Arratia, Characterizing elastic turbulence in channel flows at low Reynolds number, *Phys. Rev. Fluids* **2**, 083302 (2017).
- [62] L. Pan, A. Morozov, C. Wagner, and P. E. Arratia, Nonlinear Elastic Instability in Channel Flows at Low Reynolds Numbers, *Phys. Rev. Lett.* **110**, 174502 (2013).
- [63] D. Kawale, E. Marques, P. L. Zitha, M. T. Kreutzer, W. R. Rossen, and P. E. Boukany, Elastic instabilities during the flow of hydrolyzed polyacrylamide solution in porous media: Effect of pore-shape and salt, *Soft Matter* **13**, 765 (2017).
- [64] D. Kawale, G. Bouwman, S. Sachdev, P. L. Zitha, M. T. Kreutzer, W. R. Rossen, and P. E. Boukany, Polymer conformation during flow in porous media, *Soft Matter* **13**, 8745 (2017).

- [65] Y. Lam, H. Gan, N.-T. Nguyen, and H. Lie, Micromixer based on viscoelastic flow instability at low Reynolds number, *Biomicrofluidics* **3**, 014106 (2009).
- [66] N. P. Teclamarium, V. A. Beck, E. S. Shaqfeh, and S. J. Muller, Dynamics of DNA polymers in post arrays: Comparison of single molecule experiments and simulations, *Macromolecules* **40**, 3848 (2007).
- [67] J. Zilz, R. Poole, M. Alves, D. Bartolo, B. Levaché, and A. Lindner, Geometric scaling of a purely elastic flow instability in serpentine channels, *J. Fluid Mech.* **712**, 203 (2012).
- [68] F. J. Galindo-Rosales, L. Campo-Deaño, F. Pinho, E. Van Bokhorst, P. Hamersma, M. S. Oliveira, and M. Alves, Microfluidic systems for the analysis of viscoelastic fluid flow phenomena in porous media, *Microfluid. Nanofluid.* **12**, 485 (2012).
- [69] V. Ribeiro, P. Coelho, F. Pinho, and M. Alves, Viscoelastic fluid flow past a confined cylinder: Three-dimensional effects and stability, *Chem. Eng. Sci.* **111**, 364 (2014).
- [70] A. Lanzaro and X.-F. Yuan, Effects of contraction ratio on nonlinear dynamics of semi-dilute, highly polydisperse PAAm solutions in microfluidics, *J. Non-Newtonian Fluid Mech.* **166**, 1064 (2011).
- [71] A. Lanzaro and X.-F. Yuan, A quantitative analysis of spatial extensional rate distribution in nonlinear viscoelastic flows, *J. Non-Newtonian Fluid Mech.* **207**, 32 (2014).
- [72] A. Lanzaro, Z. Li, and X.-F. Yuan, Quantitative characterization of high molecular weight polymer solutions in microfluidic hyperbolic contraction flow, *Microfluid. Nanofluid.* **18**, 819 (2015).
- [73] A. Lanzaro, D. Corbett, and X.-F. Yuan, Nonlinear dynamics of semi-dilute PAAm solutions in a microfluidic 3D cross-slot flow geometry, *J. Non-Newtonian Fluid Mech.* **242**, 57 (2017).
- [74] S. J. Haward, C. C. Hopkins, and A. Q. Shen, Asymmetric flow of polymer solutions around microfluidic cylinders: Interaction between shear-thinning and viscoelasticity, *J. Non-Newtonian Fluid Mech.* **278**, 104250 (2020).
- [75] S. J. Haward, N. Kitajima, K. Toda-Peters, T. Takahashi, and A. Q. Shen, Flow of wormlike micellar solutions around microfluidic cylinders with high aspect ratio and low blockage ratio, *Soft Matter* **15**, 1927 (2019).
- [76] S. Aramideh, P. P. Vlachos, and A. M. Ardekani, Nanoparticle dispersion in porous media in viscoelastic polymer solutions, *J. Non-Newtonian Fluid Mech.* **268**, 75 (2019).
- [77] S. De, P. Krishnan, J. van der Schaaf, J. Kuipers, E. Peters, and J. Padding, Viscoelastic effects on residual oil distribution in flows through pillared microchannels, *J. Colloid Interface Sci.* **510**, 262 (2018).
- [78] S. De, S. Koesen, R. Maitri, M. Golombok, J. Padding, and J. van Santvoort, Flow of viscoelastic surfactants through porous media, *AIChE J.* **64**, 773 (2018).
- [79] S. De, J. Kuipers, E. Peters, and J. Padding, Viscoelastic flow simulations in random porous media, *J. Non-Newtonian Fluid Mech.* **248**, 50 (2017).
- [80] S. De, J. A. M. Kuipers, E. A. J. F. Peters, and J. T. Padding, Viscoelastic flow simulations in model porous media, *Phys. Rev. Fluids* **2**, 053303 (2017).
- [81] S. De, J. van der Schaaf, N. Deen, J. A. M. Kuipers, E. A. J. F. Peters, and J. T. Padding, Lane change in flows through pillared microchannels, *Phys. Fluids* **29**, 113102 (2017).
- [82] F. Babayekhorasani, D. E. Dunstan, R. Krishnamoorti, and J. C. Conrad, Nanoparticle dispersion in disordered porous media with and without polymer additives, *Soft Matter* **12**, 5676 (2016).
- [83] S. Kenney, K. Poper, G. Chapagain, and G. F. Christopher, Large Deborah number flows around confined microfluidic cylinders, *Rheol. Acta* **52**, 485 (2013).
- [84] S. Varchanis, C. C. Hopkins, A. Q. Shen, J. Tsamopoulos, and S. J. Haward, Asymmetric flows of complex fluids past confined cylinders: A comprehensive numerical study with experimental validation, *Phys. Fluids* **32**, 053103 (2020).
- [85] M. Avgousti and A. N. Beris, Nonaxisymmetric modes in viscoelastic Taylor-Couette flow, *J. Non-Newtonian Fluid Mech.* **50**, 225 (1993).
- [86] R. Sureshkumar, A. N. Beris, and M. Avgousti, Nonaxisymmetric subcritical bifurcations in viscoelastic Taylor-Couette flow, *Proc. R. Soc. London A* **447**, 135 (1994).
- [87] K.-W. Hsiao, C. Sasmal, J. Ravi Prakash, and C. M. Schroeder, Direct observation of DNA dynamics in semidilute solutions in extensional flow, *J. Rheol.* **61**, 151 (2017).
- [88] N. François, D. Lasne, Y. Amarouchene, B. Lounis, and H. Kellay, Drag Enhancement with Polymers, *Phys. Rev. Lett.* **100**, 018302 (2008).

- [89] Y. Liu, Y. Jun, and V. Steinberg, Longest relaxation times of double-stranded and single-stranded DNA, *Macromolecules* **40**, 2172 (2007).
- [90] C. M. Schroeder, H. P. Babcock, E. S. Shaqfeh, and S. Chu, Observation of polymer conformation hysteresis in extensional flow, *Science* **301**, 1515 (2003).
- [91] H. P. Babcock, R. E. Teixeira, J. S. Hur, E. S. Shaqfeh, and S. Chu, Visualization of molecular fluctuations near the critical point of the coil- stretch transition in polymer elongation, *Macromolecules* **36**, 4544 (2003).
- [92] J. S. Hur, E. S. Shaqfeh, H. P. Babcock, D. E. Smith, and S. Chu, Dynamics of dilute and semidilute DNA solutions in the start-up of shear flow, *J. Rheol.* **45**, 421 (2001).
- [93] D. E. Smith and S. Chu, Response of flexible polymers to a sudden elongational flow, *Science* **281**, 1335 (1998).
- [94] T. T. Perkins, D. E. Smith, and S. Chu, Single polymer dynamics in an elongational flow, *Science* **276**, 2016 (1997).
- [95] P. J. Oliveira, An exact solution for tube and slit flow of a FENE-P fluid, *Acta Mech.* **158**, 157 (2002).
- [96] B. Purnode and M. J. Crochet, Polymer solution characterization with the FENE-P model, *J. Non-Newtonian Fluid Mech.* **77**, 1 (1998).
- [97] R. B. Bird, P. J. Dotson, and N. L. Johnson, Polymer solution rheology based on a finitely extensible bead-spring chain model, *J. Non-Newtonian Fluid Mech.* **7**, 213 (1980).
- [98] M. D. Chilcott and J. M. Rallison, Creeping flow of dilute polymer solutions past cylinders and spheres, *J. Non-Newtonian Fluid Mech.* **29**, 381 (1988).
- [99] H. Jasak, A. Jemcov, and Z. Tukovic, Openfoam: A C++ library for complex physics simulations, *Proceedings of the International Workshop on Coupled Methods in Numerical Dynamics* (IUC, Dubrovnik, Croatia, 2007), p. 1.
- [100] F. Pimenta and M. A. Alves, Stabilization of an open-source finite-volume solver for viscoelastic fluid flows, *J. Non-Newtonian Fluid Mech.* **239**, 85 (2017).
- [101] J. L. Favero, A. R. Secchi, N. S. Cardozo, and H. Jasak, Viscoelastic flow analysis using the software OpenFOAM and differential constitutive equations, *J. Non-Newtonian Fluid Mech.* **165**, 1625 (2010).
- [102] See Supplemental Material at <http://link.aps.org/supplemental/10.1103/PhysRevFluids.6.033304> for supplementary videos.
- [103] L. E. Rodd, T. P. Scott, D. V. Boger, J. J. Cooper-White, and G. H. McKinley, The inertio-elastic planar entry flow of low-viscosity elastic fluids in micro-fabricated geometries, *J. Non-Newtonian Fluid Mech.* **129**, 1 (2005).
- [104] B. Khomami and L. D. Moreno, Stability of viscoelastic flow around periodic arrays of cylinders, *Rheol. Acta* **36**, 367 (1997).
- [105] K. Arora, R. Sureshkumar, and B. Khomami, Experimental investigation of purely elastic instabilities in periodic flows, *J. Non-Newtonian Fluid Mech.* **108**, 209 (2002).
- [106] S. J. Haward, K. Toda-Peters, and A. Q. Shen, Steady viscoelastic flow around high-aspect-ratio, low-blockage-ratio microfluidic cylinders, *J. Non-Newtonian Fluid Mech.* **254**, 23 (2018).
- [107] S. J. Haward, G. H. Mckinley, and A. Q. Shen, Elastic instabilities in planar elongational flow of monodisperse polymer solutions, *Sci. Rep.* **6**, 33029 (2016).
- [108] R. J. Poole, M. A. Alves, and P. J. Oliveira, Purely Elastic Flow Asymmetries, *Phys. Rev. Lett.* **99**, 164503 (2007).
- [109] G. N. Rocha, R. J. Poole, M. A. Alves, and P. J. Oliveira, On extensibility effects in the cross-slot flow bifurcation, *J. Non-Newtonian Fluid Mech.* **156**, 58 (2009).
- [110] S. J. Haward and G. H. McKinley, Instabilities in stagnation point flows of polymer solutions, *Phys. Fluids* **25**, 083104 (2013).
- [111] S. Kokal and A. Al-Kaabi, Enhanced oil recovery: challenges and opportunities, *Glob. Energy Solut.* **64**, 64 (2010).
- [112] P. Naik, S. Aramideh, and A. M. Ardekani, History matching of surfactant-polymer flooding using polynomial chaos expansion, *J. Pet. Sci. Eng.* **173**, 1438 (2019).
- [113] P. Naik, P. Pandita, S. Aramideh, I. Bilonis, and A. M. Ardekani, Bayesian model calibration and optimization of surfactant-polymer flooding, *Comput. Geosci.* **23**, 981 (2019).

- [114] S. Aramideh, P. P. Vlachos, and A. M. Ardekani, Unstable displacement of non-aqueous phase liquids with surfactant and polymer, [Transp. Porous Media](#) **126**, 455 (2019).
- [115] S. Aramideh, R. Borgohain, P. K. Naik, C. T. Johnston, P. P. Vlachos, and A. M. Ardekani, Multi-objective history matching of surfactant-polymer flooding, [Fuel](#) **228**, 418 (2018).
- [116] S. Aramideh, P. P. Vlachos, and A. M. Ardekani, Pore-scale statistics of flow and transport through porous media, [Phys. Rev. E](#) **98**, 013104 (2018).
- [117] J. Towns, T. Cockerill, M. Dahan, I. Foster, K. Gaither, A. Grimshaw, V. Hazlewood, S. Lathrop, D. Lifka, G. Peterson, R. Roskies, J. Scott, and N. Wilkins-Diehr, Xsede: Accelerating scientific discovery, [Comput. Sci. Eng.](#) **16**, 62 (2014).
- [118] P. J. Oliveira, Asymmetric flows of viscoelastic fluids in symmetric planar expansion geometries, [J. Non-Newtonian Fluid Mech.](#) **114**, 33 (2003).